# Fluid Flow Characteristics of a Swirl Jet Impinging on a Flat Plate

## Juliana K. Abrantes[1], Luis Fernando A. Azevedo[2]

1: Department of Mechanical Engineering, PUC-Rio, Rio de Janeiro, Brazil, kuhlmann@mec.puc-rio.br
2: Department of Mechanical Engineering, PUC-Rio, Rio de Janeiro, Brazil, Lfaa@mec.puc-rio.br

**Abstract**   The flow characteristics of a swirling jet flow impinging on a flat plate were investigated experimentally. Instantaneous Particle Image Velocimetry (PIV) and Laser Doppler Velocimetry (LDV) were employed to capture detailed information on the axial, radial and circumferential components of the turbulent velocity field. The configurations investigated corresponded to a Reynolds number of 21000 and jet-to-plate distances of 2 and 0.25 times the jet diameter. Time-averaged distributions of the local heat transfer coefficient were also obtained for a constant heat flux thermal boundary condition. The mean and instantaneous velocity maps obtained for this configuration revealed that a vortical structure is present at the impinging surface for the highest value of the swirl intensity investigated, and for the larger spacing. This complex recirculating structure was shown to significantly influence the stagnation Nusselt number. Peaks in the radial Nusselt number distribution were observed and linked to peaks in the measured turbulent velocity close to the plate.

## 1. Introduction

Jets impinging on surfaces produce the highest heat and mass transfer coefficients attainable for single phase flow. For that reason, they are widely encountered in different industrial applications, such as drying of paper and fabrics, heating and cooling of metals, glass tempering, localized cooling of high power electronic components, and turbine blade cooling. Besides its practical importance, jets impinging on solid surfaces have also received considerable attention in the literature because its simple geometry presents several flow types of interest. Indeed, in the impinging jet flow configuration one finds a potential core, a stagnation zone, shear layers and developing wall jets. These are all rich flow patterns from the fundamental point of view, especially for the turbulent regime. Because of that, jets impinging on solid surfaces have been used to assess the predicting capabilities of computational codes and turbulence models (Cooper et al., 1993).

A review of the literature shows a significant number of studies of the classical non-swirling jet impingement configuration. The papers of Martin (1977) and Downs and James (1987) review the studies conducted presenting the influence on the mass and heat transfer characteristics of a number of parameters. Among the works cited, special mention should be given to the pioneer work of Gardon and Akfirat (1965) where small heat flux gages were developed and used for measuring, for the first time, the radial variation of the Nusselt number. The peaks observed in the Nusselt number distribution were associated to peaks in the turbulence intensity distribution at the impinged wall. New computational and experimental tools have been used to reveal details of the flow field and heat/mass transfer characteristics of impinging jets. As examples of these more recent investigations, we can cite the work of Lyttle and Webb (1994), and the works of Azevedo et al. (1997), Fairweather and Hargrave (2002),and Geers et al. (2004).

The first reference to swirling impinging jets found in the literature is in the work of Martin (1977). In this review work, the author mentions that the presence of the circumferential velocity component does not produce significant changes on the heat or mass transfer from the wall. Ward and Mahmood (1982), however, presented different conclusions, indicating that the presence of the swirl flow significantly reduces the heat or mass transfer from the wall. Motivated by this contradiction in the literature, Almeida and Azevedo (1995) and   Azevedo et al. (1997) employed the naphthalene sublimation technique to demonstrate that, in general, the presence of the

circumferential velocity component acts as to decrease the average transfer coefficients as compared to the non-swirling base case. In particular, the authors verified a significant reduction of the mass transfer coefficients at the jet stagnation region. This decrease was credited to the decrease of the jet axial velocity with increasing swirl intensity. One of the most interesting results presented in these works was the identification of zones of recirculating flow at the jet stagnation region. Although only the footprints of these zones were registered by the surface visualization technique employed, the authors suggested that a toroidal vortex was present at the stagnation region. Recently, Nozaki et al. (2003) combined whole field velocity and temperature measuring techniques (PIV and LIF) to investigate swirl impinging jets. The work was conducted for a small value of the jet Reynolds number, namely 4000. The results confirmed the presence of the recirculating zone at the stagnation region, and relate the heat transfer behavior to the dynamic character of this zone.

This brief literature review demonstrated that there are still very few studies conducted on the fluid flow and heat transfer characteristics of swirl flow jet impingement. In the present work, a detailed investigation of swirl jet impingement operating in the turbulent flow regime was conducted. The flow field was characterized by both PIV and LDV techniques. Local heat transfer measurements were also obtained using the same test section employed in the fluid flow tests, which is a desirable feature that allows proper correlation of fluid flow and heat transfer results. Detailed information on the average and instantaneous behavior of the flow was obtained, which can also be used for future validation of computational models. As will be shown along the text, the presence of the circumferential component may produce significant changes on the structure of the flow with direct impact on its heat and mass transfer characteristics.

## 2. Experiments

The fluid flow and heat transfer measurements were conducted in the same test section presented schematically in Fig.1. Since the fluid flow measuring techniques employed required the use of seeding particles, the test section was designed to produce a jet flow by suction. In this way, the seeding particles could be easily ducted out of the laboratory space.
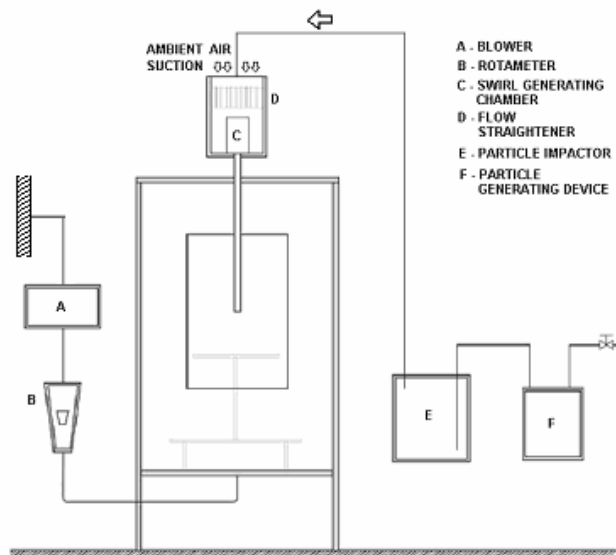


Figure 1 – Schematic view of the test section

As Figure 1 shows, air sucked by a blower at the lower part of a large tank was forced to enter at the top of the tank forming the jet. The interior dimensions of the tank were 900 x 600 x 600 mm (height x width x depth). The air entering the tank had to pass through a flow straightener section, through a swirl generating chamber, and through the test pipe. After leaving the test pipe, the air impinged orthogonally on a 300-mm-diameter glass flat plate. The glass plate was mounted on a telescopic support that allowed both leveling of the plate and the adjustment of the jet-to-plate distance. It is important to mention that, for the non-swirl case, the length of the pipe was not large enough to provide fully developed velocity and turbulence profiles. The jet diameter was 22 mm and the pipe was 300 mm long. The swirl generating chamber was formed by a vertical thick-walled brass tube closed at its top end and open at its bottom end. At the lateral surface of this tube, eight columns of 25 holes were drilled, equally spaced circumferentially. With this geometry, air sucked by the blower penetrated tangentially in the generating chamber producing the desired swirl flow that entered into the jet pipe. The swirl intensity could be adjusted by placing extra plastic pipe spools after the generating chamber. The seeding particles used in the experiments were olive oil droplets with diameter in the 1-3 μm range. The droplets were generated by a set of four Laskin nozzles driven by compressed air from the laboratory, designed as described in Raffel et al. (1998), or Abrantes (2005). After leaving the generating unit, the air stream carrying the droplets was passed through an impactor plate unit to remove the larger diameter droplets, and was finally conducted to the top of the circular chamber and into the jet. The air flow rate through the jet pipe was measured by a calibrated rotameter. The flow rate was adjusted by controlling the speed of the electrical motor that drove the blower by means of a frequency inverter.

## Velocity Measurement*s*

Two different techniques were employed to measure the fluid flow characteristics in the swirl jet impingement experiments. Instantaneous, whole field measurements were obtained by using a Particle Image Velocimetry system, while point measurements of mean and fluctuating velocity components were obtained by a Laser Doppler Velocimetry system. The combined use of both techniques produced valuable complementary information. Indeed, the PIV technique produces information on extensive regions of the flow, which is ideal for capturing the instantaneous nature of the flow field. However, with the measuring system employed in the experiments, the data acquisition rate was limited to 15 Hz by the pulsing frequency of the lasers. For the LDV system, data rates of up to 5 kHz are easily attainable for a particular point in the flow which is ideal for computing point flow statistics.

### *Particle Image Velocimetry – PIV*

The PIV technique is based on the measurement of the displacement of seeding particles distributed in the flow and illuminated by a planar sheet of pulsating laser light. The in-plane, two-dimensional displacement field of a small group of particles is determined by conveniently processing the images obtained. The PIV system used was manufactured by TSI Inc. The system employed a New Wave Research, 120 mJ per pulse, double-cavity laser that is able to fire double pulses at 15 Hz. The tracer particles used were the 1-3 μm-diameter olive oil droplets already described. The CCD camera used to capture the particle images (TSI model PIVCAM 10-30) had a 1000 x 1000 pixel resolution, working at 30 frames per second. This camera was mounted on a three-dimensional coordinate table with resolution of 0.01 mm in each direction. Synchronization between laser firing and image capturing was accomplished by a TSI model 60030 synchronizer. A cross-correlation-based algorithm was employed to determine the particle displacement field. A recursive technique was employed to obtain high resolution vector fields by successively decreasing the interrogation window. Each instantaneous image was composed of approximately 15000 vectors. The dimensions of the field of view were set so as to minimize bias errors in the calculation

of the fluctuating velocity components. One important source of errors, known in the literature as pixel locking, is derived from the discrete resolution of the particle displacements when imaged by a discrete array such as a CCD sensor. These errors are minimized by setting the experiment so that particle image occupies at least two to three pixels in the image sensor (Christensen, 2004). Also, when the circumferential velocity component is superimposed on the flow, the tracer particles cross the light sheet at significant velocities. In order to be able to measure the in-plane velocity components it is necessary to work with small time intervals between laser pulses. In the present case, time intervals of the order of 5 μs were used with success. In order to obtain time-averaged fields, over 2000 images were captured and averaged. Turbulent quantities such as RMS velocity fields were obtained by subtracting from each instantaneous field, the average field. In order to obtain information on the flow field away from the stagnation zone, measurements were taken by moving the coordinate table that supported the camera along the transverse (radial) direction.

*Laser Doppler Velocimetry – LDV*

Local, time-resolved velocity measurements were conducted employing a two-component laser Doppler velocimetry system made by TSI Inc. The system was composed of a two-color, fiber-optic-based, four-beam probe, that produced a measuring volume with dimensions of 100 x 250 μm, with a focal length of 350 mm. Both beams could be frequency shifted. The light scattered by the tracer particles was converted into electrical signal and processed by an IFA 750 signal processor. Turbulent information was obtained by post-processing the data using the FIND software developed by TSI Inc. A 5W Coherent Argon-ion laser was used in the experiments. Seeding was provided by the same system already described for the PIV measurements. Typically, velocity data was acquired during 20 seconds at a rate of about 3000 samples per second. The optical probe was mounted on the same coordinate table used for the PIV experiments.

*Heat Transfer Measurements*

The test section described previously was designed to also allow the measurement of time-averaged, local heat transfer coefficients along the plate. All the test section elements employed in the fluid flow measurements were utilized in the heat transfer experiments, with the exception of the impinging plate. For the heat transfer measurements, the glass plate was substituted by a 400 x 400 mm sandwich plate. The plate was formed by a 5-mm-thick Celeron plate bolted to a 12-mm-thick Plexiglas frame. Between the Celeron plate and the Plexiglas frame, a 25-mm-thick Styrene plate was inserted to minimize heat losses. The heating element was a 0.025-mm-thick Nichrome foil with dimensions of 200 x 500 mm (width x length) cemented to the Celeron plate. The edges of the foil were connected to a DC power supply, thereby producing a constant heat flux thermal boundary condition for the experiments. Seventy, 0.075-mm-diameter, Chromel-Constantan thermocouples were installed at the back surface of the heating element foil. The thermocouples were installed through holes previously drilled into the Celeron plate. A thermal conducting cement was used to secure the thermocouples in position. An alignment procedure was conducted prior to each data run to guarantee that the centerline of the jet pipe was positioned directly above the center thermocouple. A second set of thermocouples was used to verify the circumferential symmetry of the data. The readings of the thermocouples were only taken at steady state condition by an Agilent 6491 data acquisition system.

## 3. Data Reduction Procedure

The swirl jet impingement heat transfer and fluid flow are characterized by three main parameters: the jet Reynolds number, the dimensionless jet-to-plate distance and the Swirl number. The shape and turbulence intensity level of the velocity profile leaving the pipe are also relevant. The Reynolds $Re$ number was evaluated directly from the volume flow measurement and nozzle diameter, $Re = \rho\, U_j\, d\, /\, \mu\, =\; 4\, \rho\, Q\, /\, \pi\, d\, \mu$, where $Q$ is the volume flow rate, $\rho$ is the air density, $d$ is the jet diameter, $U_j$ is the jet exit average velocity, and $\mu$ is the air dynamic viscosity.

The swirl intensity is characterized by the Swirl number, $S$, the ratio of the flow angular momentum flux, $G_\varphi$, divided by the axial linear momentum flux, $G_x$, multiplied by the jet radius, $R$. Thus,

$$S = G_\varphi\, /\, R\; G_x\,, \quad \text{with} \quad G_\varphi\, =\, 2\pi \int \rho\, \overline{U}\,\overline{W}\, r^2 dr\,, \quad \text{and} \quad G_x\, =\, 2\pi\rho \int \overline{U}^2 r dr \tag{1}$$

where, $\overline{U}$ and $\overline{W}$ are, respectively, the time averaged axial and circumferential components of the fluid velocity measured by the LDV at the jet exit.

The local Nusselt number was evaluated by dividing the local heat flux per unit area delivered by the heating foil, $q''$, by the local wall-to-fluid temperature difference, $(T(r) - T_j)$, and multiplying it by the ratio of jet diameter to the air thermal conductivity, $k$. The heat losses by radiation from the foil surface and by conduction through the back insulation were estimated to be negligible. Thus,

$$Nu(r) = q''d \,\big/ \left[\left(T(r) - T_j\right)k\right] \tag{2}$$

## 4. Results and Discussion

The flow field and local heat transfer results obtained will be presented next. The presentation starts with the results for a dimensionless jet-to-plate distance $H/d =2$. Following, the results for the smaller spacing $H/d = 0.25$ are explored. All the information presented corresponds to a Reynolds number of 21000, and for two values of the Swirl number, $S$=0 (non-swirl case) and $S$=0.5 (maximum swirl case).

Figure 2 presents instantaneous velocity fields and time-averaged velocity magnitude contours in the $y$-$r$ plane, in the vicinity of the stagnation region, obtained with the PIV technique. The figures allow an assessment of the effect of the swirl flow component on the flow field. The results presented correspond to $H/d = 2$ and $Re = 21000$, for the non-swirl and maximum swirl cases. In the figures, the top border corresponds to the jet exit plane, while the lower border coincides with the impinging plate. The left border of the figure coincides with the jet symmetry axis.

Figure 2(a) shows an instantaneous velocity field for $S$=0, where the turbulent nature of the flow can be observed. An observation of a sequence of these figures clearly shows the continuous generation and transport of vortical structures characterizing the development of a shear layer at the jet interface. A comparison of this flow pattern with the one presented in Figure 2(c) for $S$=0.5 shows a remarkable difference. The most striking difference is the spreading of the jet in the radial direction caused by the presence of the swirl. Indeed, the jet is seen to practically maintain its width for the non-swirl case as it develops from the jet exit plane to the impinging plate, while a significant spread is verified for $S$=0.5, which causes the displacement of the impingement point forward in the radial direction. After this point, a wall-jet-type structure is formed. The spreading of the jet causes a decrease in the levels of axial velocity in the center of the jet, leading to the

formation of zones of recirculating flow in the jet core, and giving rise to a second shear layer at the interface of the jet with this inner slow-moving-fluid region, where intense vortices are formed.

The zones of recirculating flow formed at the stagnation region can be better identified by observing the time-averaged velocity magnitude contours presented in Figures 2(b) and (d). The white lines in these figures represent the projection on the y-r plane of fluid particle trajectories. For the case of $S = 0.5$ depicted in Figure 2(d), these lines can not be interpreted as streamlines due to the three dimensional nature of the mean flow field caused by the presence of the swirl flow. In Figure 2(d) the zones of recirculating flow are clearly identifiable. In fact, the presence of two zones of recirculating flow within the jet core can be identified. The shift on the location of the maximum velocity magnitude toward the region of the jet pipe wall wake caused by the swirl flow component can also be observed in the figure. The presence of zones of recirculation in the jet core has been documented indirectly in the experiments of Almeida et al. (1997) and more recently by Nozaki et al. (2003).
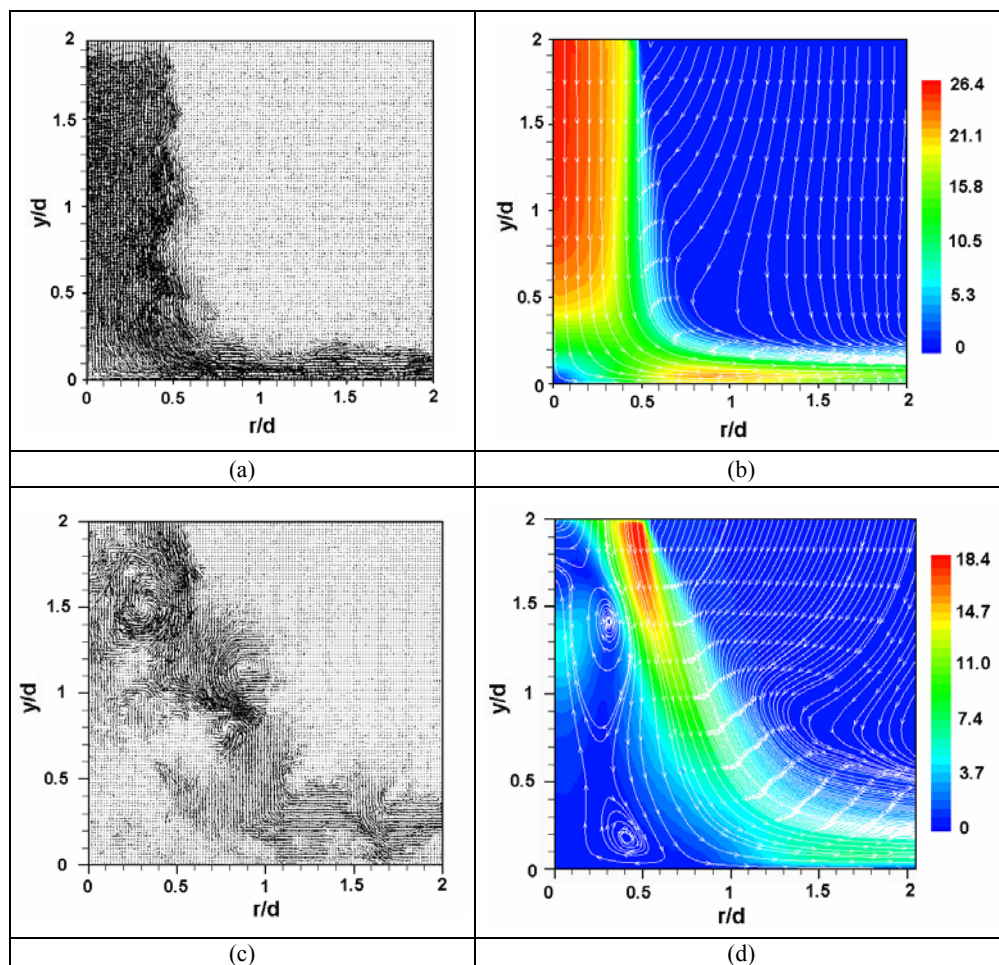


Figure 2 – Instantaneous velocity fields, $Re$=21000, $H/d$=2: (a) $S$=0; (c) $S$=0.5; Time-averaged velocity magnitude contours [m/s], $H/d$=2: (b) $S$=0; (d) $S$=0.5

The contour map of Figure 2(b) also allows us to visualize the severe deceleration suffered by the fluid as it approaches the impinging plate, in the case of no-swirl. It is seen that in this case the core of the jet maintains its approximate maximum speed up to a distance of about half diameter

from the wall, from where it is decelerated to zero velocity at the wall. An examination of Figure 2(d) shows that the presence of the swirl flow component not only decreases the maximum jet velocity as compared to the non-swirl case, but also significantly reduces the velocity gradients prevailing at or near the stagnation region.

The experimental results obtained also allowed the observation of the flow as it develops in regions away from the stagnation zone, at larger values of the radial coordinate, *r*. These results were obtained by horizontally traversing the PIV camera. Figures 3, 4 and 5 present contours of mean velocity magnitude (formed by axial and radial components) and turbulent velocities for the non-swirl and swirl cases. In all cases, *Re*=21000 and *H/d*=2. The contours of time-averaged velocity magnitude presented in figure 3(a) and (b) show that, besides the significant differences in the stagnation region already commented, the wall jet structure is weakened for the swirling case, probably due to the presence of the circumferential velocity component. Figures 4(a) and (b) present the contours of axial turbulent RMS velocity. For the non-swirl case, the results show that the region of more intense axial RMS velocity is located downstream of the jet pipe wall, at about *r/d*=0.5. For the swirl case, this region is still downstream of the jet exit plane but has been shifted towards the jet centerline for a position around *r/d*=0.3. This region of higher axial RMS velocity intensity is probably a consequence on the action of the two shear layers developing around the jet boundaries, one at the interface of the jet with the surrounding stagnant fluid, and the other at the interface of the jet with the slow moving fluid of the inner recirculating zone. For the rest of the field, the presence of the wall seems to dump the axial turbulent velocity in a similar way for the swirl and non-swirl cases. In the case of the radial turbulent RMS velocity, the results presented in Figures 5(a) and (b) demonstrate that, while the peak intensity for the swirl case is located at the region immediately downstream of the jet exit plane, in the non-swirl case it is found close to the impinging wall, at the initial stages of the developing wall jet. This is probably due to the combined action of the shear layer at the interface of the wall jet with the surrounding air, and the turbulence generated by the sharp turning of the jet at that region.
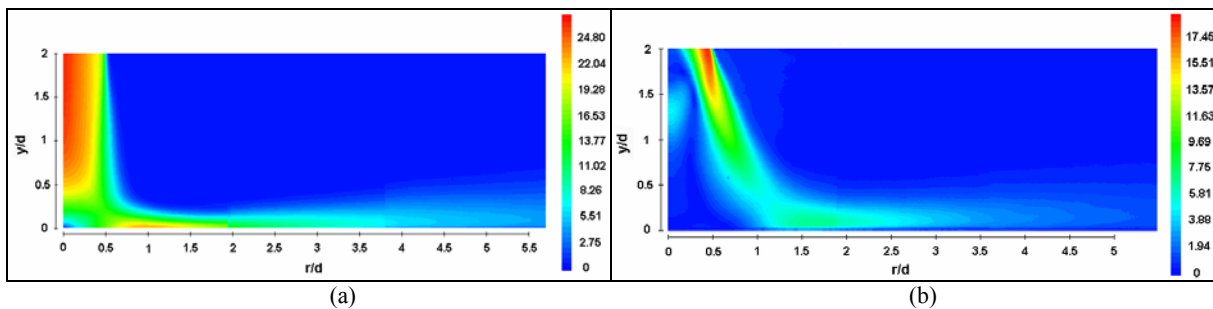


(a) (b)

Figure 3 – Time-averaged velocity magnitude contours, $\sqrt{\overline{U}^2 + \overline{V}^2}$, [m/s]. *Re*=21000, *H/d*=2
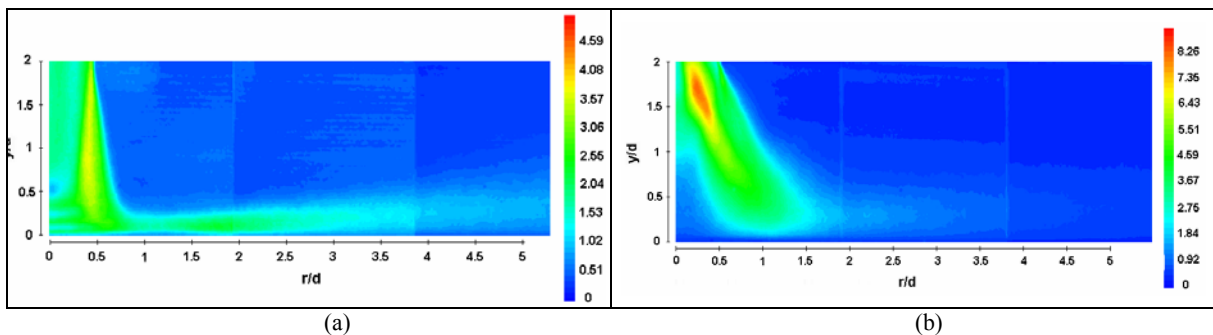(a) *S*=0 (b) *S*=0.5



(a) (b)

Figure 4 – Axial turbulent RMS velocity contours - *u'* [m/s]. *Re*=21000, *H/d*=2
(a) *S*=0; (b) *S*=0.5

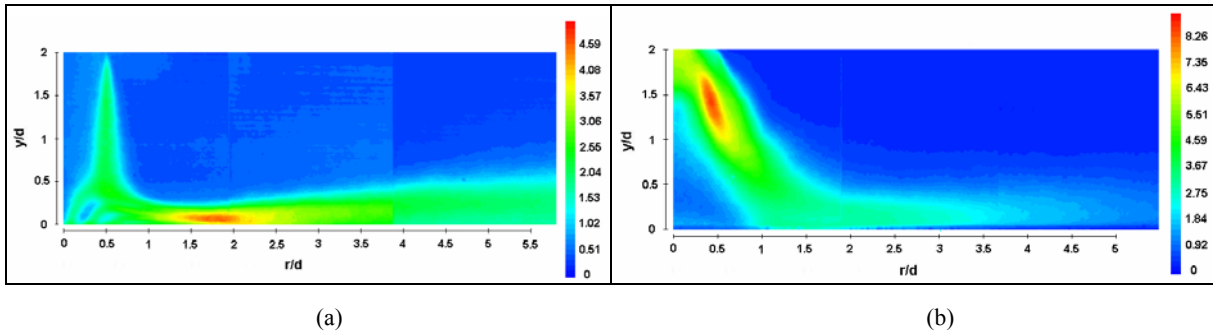(a)                                                                              (b)

Figure 5 – Radial turbulent RMS velocity contours - *v'* [m/s]. *Re*=21000, *H/d*=2
(a) *S*=0; (b) *S*=0.5

Figures 6(a) and (b) were prepared to convey a better quantitative comparison of the turbulent velocities for the swirl and non-swirl cases close to the impinging wall. Figure 6(a) shows the axial and radial turbulent dimensionless RMS velocities for the non-swirl case, while Figure 6(b) displays the same information for *S*=0.5. Figure 6(b) also includes data on the turbulent velocity in the circumferential direction measured with the LDV system. All these values presented in Figure 6 were measured at a vertical coordinate very close to the plate surface, namely, *y* = 0.02*d*. Results of turbulence intensity close to the wall are relevant to help understand the heat transfer characteristics of the jet impingement configuration.

The results of Figure 6 show that, as expected, the radial components of the turbulent velocities for the swirl and non-swirl cases are higher than the axial components, damped by the wall at this small value of the vertical coordinate. Also, the peaks in the radial component distributions are of similar magnitude regardless of the presence of the swirl component. The turbulent circumferential velocity for the swirl case is seen to be of the same order of magnitude as the radial component, although it appears to reach its maxima and start decaying at a smaller radial coordinate. Since the three components of the turbulent velocity were measured for the swirl case, it was possible to compute the turbulent kinetic energy distribution along the radial coordinate for that particular vertical coordinate. The turbulent kinetic energy was calculated by $k = (u'^2+v'^2+w'^2)/2$, and it is presented in Figure 6(b) in its dimensionless form, *Uj* being the jet mean exit velocity.
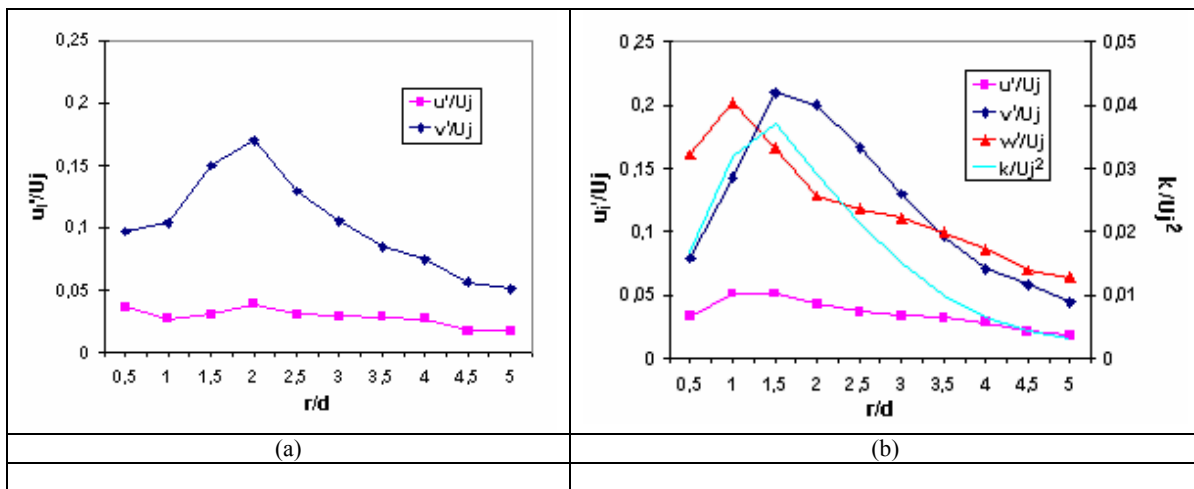


(a)                                                                              (b)

Figure 6 – Profiles of RMS velocities and turbulent kinetic energy at *y* = 0.02 *d*. *H/d* = 2
(a)   *S*=0; (b) *S*=0.5.

The results obtained for the time-averaged, local heat transfer from the impinging plate will now be presented. Figure 7 shows the radial profiles of local Nusselt number for the two values of Swirl intensity investigated ($S$=0 and $S$=0.5), and for two values of the jet-to-plate distance, namely $H/d$= 2 and 0.25. In all case the Reynolds number was 21000. These results will be discussed and explained in light of the flow characteristics previously presented.
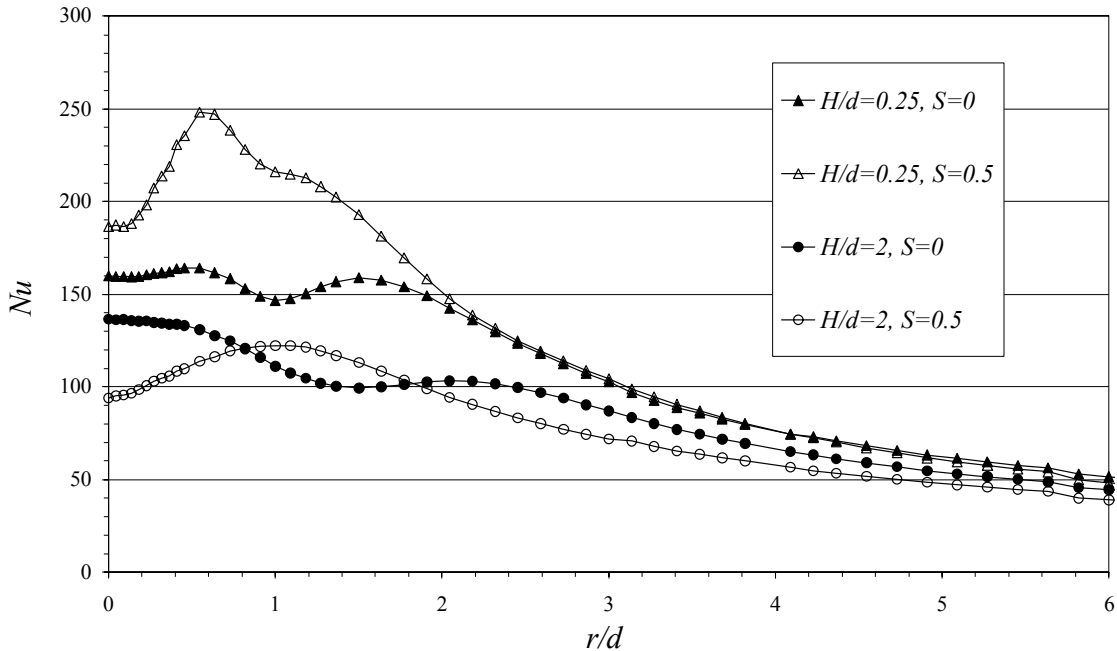


Figure 7 – Radial distribution of the local Nusselt number, $Re$=21000.

An observation of the results presented in Figure 7 reveals some trends that are well documented in the literature for non-swirl stagnation jets (e.g., Gardon and Akfirat, 1965 or Little and Webb, 1994). For instance, it is known that, for jet-to-plate distances larger than approximately 6 jet diameters, the local Nusselt distribution presents a maximum value at the stagnation region, decreasing monotonically with the radial coordinate. As seen in Figure 7, for a smaller spacing equal to $H/d$ =2, a secondary peak is developed in the radial Nu distribution, although the overall maximum is still located at the stagnation point. The position of this secondary maximum at $r/d \approx 2$ coincides with the location of the peak in the RMS radial velocity distribution measured for the same spacing and presented in Figures 5(a) and 6(a). Further reduction in the dimensionless spacing to $H/d = 0.25$ shows a plateau in the stagnation Nusselt number distribution, and an intensification of the secondary peak. Also, for this spacing, an inner peak in the Nusselt distribution is observed at about $r/d = 0.5$. The value of this peak is about the same as that for the outer maxima and slightly higher than the value at stagnation. For $H/d = 0.25$ and smaller spacings, global mass conservation imposes an acceleration on the fluid through the gap formed between the jet pipe and the impinging wall. The inner peak identified at $r/d = 0.5$ for $H/d = 0.25$ is attributed to flow acceleration in the gap. A comparison of the Nusselt distributions for the spacings presented in Figure 7 shows that the smaller spacing $H/d = 0.25$ produces higher rates of heat transfer for all radial positions.

We now turn attention to the effect of the swirl flow on the local Nusselt distribution. The data correspond to the maximum swirl intensity investigated, namely, $S = 0.5$. It can be seen in Figure 7 that the swirl flow component has a significant impact on the local heat transfer distribution. For $H/d$=2 the Nusselt distribution no longer presents a maximum at the stagnation region, as it was verified for the non-swirl case. Rather, a single maximum is now located further downstream in the radial direction at about $r/d$ =1.1. For this particular spacing, the fluid flow data presented

previously can help understand the changes in the local Nusselt distribution. One of the most significant changes produced by the swirl flow component on the flow field was shown to be the formation of a large zone of recirculating flow at the stagnation region, accompanied by the displacement of the impingement point in the radial direction. The slow moving fluid in the recirculation zone is responsible for the decrease in heat transfer, while the impingement produces the peak in the Nusselt distribution. The location of the impingement point observed in Figure 2(d) coincides with the location of the peak in Nu in Figure 7. Further, the data presented in figure 6(b), shows that the turbulent kinetic energy close to the impinging wall also peaks around this radial position, cooperating for the increase in the local heat transfer.

For the smaller spacing, $H/d = 0.25$, a different scenario for the Nusselt distribution is observed in Figure 7. The presence of the swirl flow component act as to significantly increase the local rate of heat transfer up to $r/d \approx 2$, as compared to the non-swirl case. A strong inner peak develops at about $r/d = 0.75$, and a secondary peak is present at $r/d \approx 1.2$. An increase in local Nusselt in excess of 60% is verified. The time-averaged velocity magnitude contours presented in Figures 8 and 9, respectively, for the non-swirl and swirl cases, present the flow patterns that prevail for this small jet-to-plate distance. It is seen that the global changes on the average flow in the $y$-$r$ plane produced by the presence of the swirl flow are not as significant as those observed for $H/d = 2$, presented in Figure 3. For this smaller spacing however, the increase in the stagnation Nusselt number, as compared to the case with $H/d = 2$, can be attributed to the stronger momentum of the incoming jet at these small spacings that precludes the formation of a zone of recirculating fluid at the stagnation region. Also, for the small jet-to-plate spacings, the decay of the circunferencial fluid velocity is less pronounced and it is expected to account for the increase in heat transfer observed when the swirl flow is present.
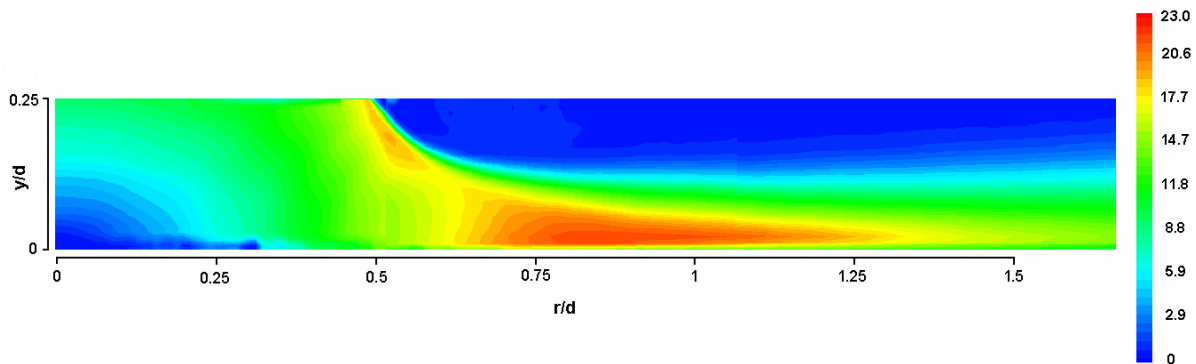


Figure 8 - Time-averaged velocity magnitude contours, $\sqrt{\overline{U}^2 + \overline{V}^2}$, [m/s]. $Re$=21000, $H/d$=0.5, $S$=0
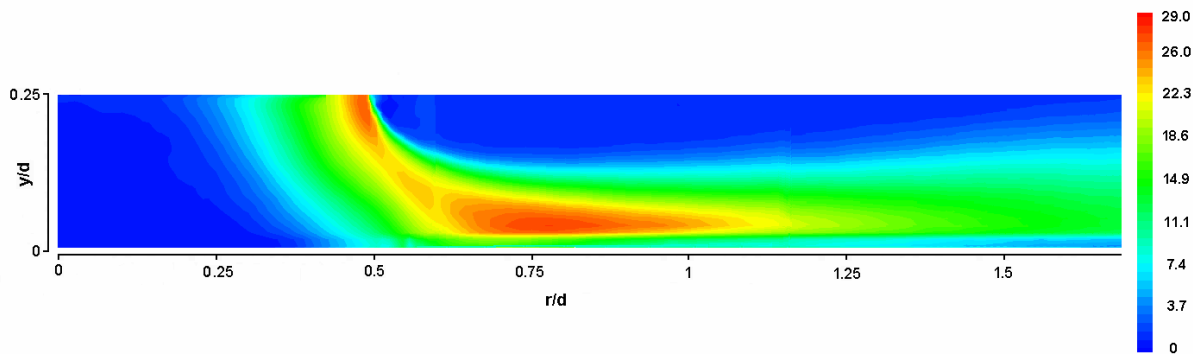


Figure 9 - Time-averaged velocity magnitude contours, $\sqrt{\overline{U}^2 + \overline{V}^2}$, [m/s]. $Re$=21000, $H/d$=0.5, $S$=0.5

## 5. Conclusions

The present work studied the fluid flow and heat transfer characteristics of a swirl jet impingement configuration. The study investigated two values of the intensity of the swirl flow, given by the swirl number, and dimensionless jet-to-plate distances of 2 and 0.25, for a Reynolds number of 21000. Instantaneous and time-averaged velocity field measurements obtained by PIV and LDV techniques produced detailed data on the mean and turbulent characteristics of the flow. Heat transfer measurements performed in the same test section produced local, time-averaged distributions of the Nusselt number.

The results revealed that the presence of the swirl velocity component produces significant impacts on the local heat transfer distribution. The changes in heat transfer could be linked to changes in the mean and fluctuating fluid flow patterns for $H/d$=2. Large zones of recirculating flow at the jet stagnation region together with the radial displacement of the impingement point were identified and shown to be correlated with the heat transfer variations. Peaks in turbulent quantities close to the impinging wall were also correlated to the heat transfer results. For the smaller spacing investigated the presence of the swirl flow component produced enhancement on the heat transfer from the plate that was linked to the stronger axial momentum of the jet at the closer plate that precluded the formation of the recirculating flow zone at the stagnation region, together with the stronger circumferential component of the jet close to the wall.

The interaction of the swirl flow component with the jet impingement configuration adds another level of difficulty to this rather complex problem. The simultaneous action of different flow mechanisms of varying intensities would require a much deeper investigation of all flow details in order to obtain a complete picture of the influence of the swirl flow on the heat transfer. Nevertheless, the partial information provided in the present paper might be useful to help understand the phenomena involved and to validate heat transfer and fluid flow computational models.

## 6. References

Abrantes, J. K., 2005, Study of flow and heat transfer characteristics in a swirling impinging jet, Master's thesis, Mechanical Engineering Department, PUC-Rio, Brazil. In Portuguese.

Almeida, J.A., Azevedo, L. F. A., 1995, Flow visualization study of swirling jet impingement, XIII Brazilian Congress of Mechanical Engineering, COBEM, Belo Horizonte, MG, Brazil (CD-ROM).

Azevedo, L. F. A., Almeida, J. A., Duarte, L. G. C., 1997, Mass transfer to swirling impinging jets, 4th World Conference on Experimental Heat Transfer, Fluid Mechanics and Thermodynamics, Editor M. Giot e Mayiner, Brussels, Belgium, 3: 1759 – 1766.

Christensen, K.T., 2004, The Influence of Peak-Locking Errors on Turbulence Statistics computed from PIV Ensembles, Experiments in Fluids, 36: 484 – 497.

Cooper, D., Jackson, D.C., Launder, B. E., Liao, G. X., 1993, Impinging Jet Studies for Turbulence Model Assessment – I. Flow Field Experiments, International Journal of Heat and Mass Transfer, 36, No. 10: 2675 – 2684.

Downs, S.J., James, E.H., 1987, Jet Impingement Heat Transfer – A Literature Survey, ASME Paper No 87 – HT – 35, American Society of Mechanical Engineers.

Fairweather, M., Hargrave, G. K., 2002, Experimental investigation of an axisymmetric, impinging turbulent jet. 1. Velocity field, Experiments in Fluids, 33, No. 3: 464 – 471.

Gardon, R., Akfirat, J.C., 1965, The Role of Turbulence in Determining the Heat Transfer Characteristics of Impinging Jets, International Journal of Heat and Mass Transfer, 8: 1261 – 1272.

Gears, L. F. G., Tummers, Hanjalic, K., 2004, Experimental Investigation of Impinging Jet Arrays, Experiments in Fluids, 36: 946 – 958.

Lyttle, D., Webb, B.W., 1994, Air jet impingement heat transfer at low nozzle-plate spacings, Int. Journal of Heat and Mass Transfer, 37: 1687 – 1697.

Martin, H., 1977, Heat and Mass Transfer Between Impinging Gas Jets and Solid Surfaces, Advances in Heat Transfer: 1-60.

Nozaki, A., Igarashi, Y. e Hishida, K., 2003, Heat Transfer Mechanism of a Swirling Impinging Jet in a Stagnation Region, Heat Transfer – Asian Research, 32, No. 8.

Raffel M., Willert C., Kompenhans J., 1998, Particle Image Velocimetry – A Practical Guide, Ed. Springer.

Ward, J., Mahmood, M., 1982, Heat Transfer from a Turbulent, Swirling, Impinging Jet, 7th Int. Heat Transfer Conference: 401 – 408.